Research Square

Preprints are preliminary reports that have not undergone peer review.
They should not be considered conclusive, used to inform clinical practice,
or referenced by the media as validated information.

Artificial Reefs: Computational Fluid Dynamics Informed Insights into Particle Interception

Oliver Kippax-Chui

o.kippax-chui23@imperial.ac.uk

Imperial College London, Royal School of Mines

Yves Plancherel

Imperial College London, Royal School of Mines

Catherine E.I. Head

Zoological Society of London

Chris Yesson

Zoological Society of London

Mark Sutton

Imperial College London, Royal School of Mines

Research Article

Keywords:

Posted Date: November 25th, 2026

DOI: https://doi.org/10.21203/rs.3.rs-11484389/v1

License: This work is licensed under a Creative Commons Attribution 4.0 International License.
Read Full License

Additional Declarations: No competing interests reported.

Artificial Reefs: Computational Fluid Dynamics Informed Insights into Particle Interception

Authors:

Oliver Kippax-Chui (0000-0003-4551-6281) [1,2,*], Yves Plancherel (0000-0002-3624-0757) [1], Catherine E.I. Head (0000-0002-5145-1632) [2,3], Chris Yesson (0000-0002-6731-4229) [2, 3], Mark Sutton (0000-0002-7137-7572) [1]

[1] Department of Earth Science & Engineering, Imperial College London, Royal School of Mines, Prince Consort Road, London SW7 2BP, UK

[2] Institute of Zoology, Zoological Society London, London, UK

[3] University College London, Gower Street, London, UK

[*] Corresponding author: o.kippax-chui23@imperial.ac.uk

Abstract

Artificial reefs (ARs) are increasingly deployed to support coral restoration, yet how their geometry influences larval settlement remains poorly quantified. Here, computational fluid dynamics (CFD) simulations of AR structures were performed and analysed with Lagrangian particle tracking to estimate collision probability on the structures. A suite of AR designs and reference geometries were simulated and oriented at varying angles to the flow to test whether structure- and vertex-scale geometric metrics can be used as predictors of collision probability.

Results show that rotating structures broadside to the flow (90°) lowers collision odds. A larger frontal area consistently reduced the likelihood of particle interception, while greater surface packing, the degree of indentation and rugosity, increased it. Surfaces on ARs that were oriented more directly toward the oncoming flow captured more particles, but the highest collision probability occurred at 2-4° rather than 0°. Convex features consistently intercepted more particles than concave ones, though the benefit of curvature showed diminishing returns, with collision probability rising to a peak near a relative curvature of 0.13 before falling off at higher curvatures. Collisions were overwhelmingly concentrated within the first few centimetres of any highly curved surface, dropping steeply with distance. Surface slope relative to the seabed had no detectable effect.

Our findings reveal a systematic trade-off between flow deflection and surface trapping that operates from the whole reef down to the centimetre scale. When prioritising initial settlement, simulation results suggest that effective ARs should balance compact from with edge-richness and convex-curved surfaces. Demonstrating the necessity of validating these insights against real world cases to determine if particle modelling informed AR design translates to real world conservation gains.

Introduction

Artificial reefs (ARs) are increasingly deployed as conservation tools to restore degraded tropical coral reef ecosystems, particularly those damaged by dynamite fishing, dredging, and

coastal development (Androulakis et al., 2020; Boström-Einarsson et al., 2020; Higgins et al., 2022; Hughes et al., 2023; Perricone et al., 2023). By providing hard substrate, they aim to recover key ecosystem services such as coastal protection, niche provision, and fish nursery habitat (A. Rahman et al., 2020; Androulakis et al., 2020; Bao et al., 2026; Carral et al., 2022; Düzbastılar and Şentürk, 2009; Galdo et al., 2022; Higgins et al., 2022; Huang et al., 2024; Jiang et al., 2016; Jiao et al., 2017; Kim et al., 2024, 2014; Lanham et al., 2025; Leftheriotis et al., 2025; Lenton, T. M. et al., 2025; Li et al., 2025; Liu and Su, 2013; Liu et al., 2013; Maslov et al., 2023; Norris et al., 2025; Perkol-Finkel et al., 2008; Riera et al., 2024, 2023; Santiago Caamaño et al., 2022; Shu et al., 2021; Vivier et al., 2021; Wang et al., 2021; Zhou et al., 2022). Their role in alleviating non climatic stressors has been highlighted in recent global tipping point assessments, which stress that removing local pressures is essential if reefs are to withstand the escalating threat of marine heatwaves (Lenton, T. M. et al., 2025). ARs fall into two broad categories. The first comprises structures designed primarily for coastal defence or fishery enhancement, true artificial reefs that serve as functional stand ins for natural reefs (Androulakis et al., 2020; Bao et al., 2026; Bordbar et al., 2025; Huang et al., 2024; Jiang et al., 2016; Kim et al., 2024; Li et al., 2025; Liu et al., 2013; Maslov et al., 2023; Riera et al., 2024; Vivier et al., 2021). The second, comprises artificial substrates deployed with the explicit intention that sessile organisms, such as coral colonies will grow on them. In the case of coral colonies usually by direct propagation of coral fragments, or, more recently, by releasing in situ fertilised or ex situ bred larvae directly onto the water column on the reef site (A. Rahman et al., 2020; Hata et al., 2017; Lanham et al., 2025; Levenstein et al., 2022; Reichert et al., 2025).

Historically, both types have been designed around resource goals rather than other considerations, such as how the shape of the structure influences water and particle movement. Research that has included hydrology, focuses on fishery relevant phenomena such as upwelling, turbulent wakes, and the resuspension of particulate organic matter (Androulakis et al., 2020; Bao et al., 2026; Bordbar et al., 2025; Huang et al., 2024; Jiang et al., 2016; Kim et al., 2024; Li et al., 2025; Liu et al., 2013; Maslov et al., 2023; Riera et al., 2024; Vivier et al., 2021). Hydrodynamics governs the transport of planktonic larvae to the reef surface (Hata et al., 2017; Kundu et al., 2025; Reichert et al., 2025), and since the initial delivery phase is passive, it is essential to know how the flow around designed structures influence collision probabilities so as to complement active settlement behaviours (chemical, acoustic, visual, pressure) that coral larvae are known to employ (Deshpande et al., 2025;

Geertsma et al., 2023; Limer et al., 2024; Ricardo et al., 2017; Rippen et al., 2025; Stake and Sammarco, 2003; Sun et al., 2025). How water flow around these structures shapes larval delivery, particularly for corals, remains poorly understood. By designing AR geometry to promote natural larval settlement, this could reduce or even eliminate the need for the labour intensive process of outplanting individual colonies, making restoration far more scalable (Reichert et al., 2025). Yet, to date, the hydrodynamic contribution of AR geometry to larval delivery has not been isolated and quantified, aside from settlement processes at the immediate substrate surface (Lanham et al., 2025; Levenstein et al., 2022). The limited work that couples flow with larval behaviour has focused on the thin boundary layer over millimetre scale textures, showing that rougher surfaces and oscillatory flow can thicken the low velocity region and improve settlement of larvae already near the substrate (Lanham et al., 2025; Levenstein et al., 2022). Rahman et al. (2020) modelled the surface pressure and vibrational characteristics of a metallic tubular sunken rig reef to infer settlement suitability. These efforts, however, all examine processes at or very near the reef surface. What remains unknown is how the variety of geometric features that exist across spatial scales around AR influences the delivery of larvae from the water column to the surface of the AR structure in the first place. This study aims to address that gap by exploring how the structure shape could promote settlement potential and thus enhance their performance as restoration tools.

The geometry of an artificial reef can be characterised at multiple scales, each of which may influence the hydrodynamic delivery of larvae in different ways. At the whole structure scale, gross morphology, planar projected surface area, and surface irregularity determine the broad flow field around the reef, whether water is deflected, channelled, or slowed (A. Rahman et al., 2020; Bao et al., 2026; Kim et al., 2014; Leftheriotis et al., 2025; Liu and Su, 2013; Zhou et al., 2022). At finer scales, individual topographic features such as curvature, slope, and the orientation of specific surface elements create local variations in flow that a settling larva would encounter (Levenstein et al., 2022; Reichert et al., 2025). It remains unclear how these geometric features operating at different spatial scales interact to modulate the probability that a planktonic larva reaches the ARs surface. Without this knowledge, it is difficult to evaluate whether structural complexity is merely an aesthetic or engineering consideration, or whether it can be deliberately manipulated to enhance larval delivery and thus settlement. Development of a formal understanding of how geometric features affect collision rates could be key to optimizing the future design of artificial reefs in a way that maximise the chances of natural settlement.

Site specific variation in bathymetry, hydrodynamics, and community composition means that no single AR design will be universally optimal. Full computational fluid dynamics (CFD) analysis, the branch of fluid mechanics that uses the Navier-Stokes equation to predict fluid flow, coupled with particle tracking can offer a physically realistic assessment of larval delivery, but computational costs and technical demands make it impractical as a routine design tool, particularly for smaller NGOs and community led restoration groups with limited computational resources or expertise. Therefore, establishing this CFD foundation within a simplified, static flume environment is imperative. These idealised, flume experiments can be used to isolate the shape elements that control collision probabilities and to identify which metrics can be used to represent and diagnose the key features of tested structures and serve as proxies to screen and compare AR designs without the need to run simulations each time.

The objectives are: (1) to compute fluid flows for 15 artificial reef designs and a set of reference shapes; (2) to quantify collision counts and identify which whole-reef features predict collision probability, and (3) to evaluate whether the combination of structural and vertex-scale features provides a coherent, cross-scale understanding of particle interception that can inform future AR design.

Methods

Software

Open source and non-commercial free-to-use software were used to create accessible tools and protocols for researchers and conservationists alike.

Three different software's were used to create the 3D mesh models of the ARs. The Fiji distribution of imageJ (version 2.15) ("Fiji," n.d.) was used as a vector-based measurement tool for extracting dimensions of ARs from reference images. For specific complicated textural surface patters the VR software Gravity Sketch ("Gravity Sketch," n.d.) was used to

trace the patterns from images into 3D space. Blender (Blender Online Community, 2018) and Meshlab (Cignoni et al., 2008) were used to create and clean the final 3D meshes of each AR.

Fluid flow simulations were performed with openFOAM v2412 (Weller et al., 1998), which was selected as it provides a suite of robust fluid solvers alongside integrated pre-processing, post-processing, and parallelisation utilities suitable for large-scale environmental flow simulations. One of the integrated tools for visualisation is called paraFOAM, an integrated replication of the visualisation software ParaView (Hansen and Johnson, 2005). Finally, the games development software Unity ("Unity," 2025) was used to develop a custom particle tracer tool, called the Coral Reef Lagrangian Settlement Simulator (CoRLSS). CoRLSS was used to simulate particle transport and collision dynamics around the AR geometries. Unity was selected due to its high degree of customisation, and capacity for real-time visualisation. While existing particle tracing tools are available within software such as ParaView, development of a bespoke framework enabled direct integration of CFD outputs, flexible particle behaviour configuration, custom collision logging functions, and flexible visualisation options. Source code for CoRLSS is available at (Sutton and Kippax-Chui, 2026).

Creation of Artificial Reef 3D Mesh Models

The dataset comprises fifteen structures representing eight distinct AR designs developed for coral reef conservation, plus two reference geometries (a cube and a sphere) included for comparison (Figure 1). Each design is identified by a numerical label (AR 1–8), while the reference shapes are labelled Cube and Sphere for clarity. Several designs include multiple variants, identified with alphabetical suffices (a, b, c, etc.). For AR 3, the intra-structure variation in size and complexity is relatively minor, so its three configurations are distinguished with alphabetical suffixes (AR 3a, b, c). In contrast, AR 7 shows a large structural difference, where one variant is a much smaller component of a full assembly in the other, these are therefore labelled descriptively as AR 7 Array and AR 7 Brick. Both AR 3 and AR 7 were modelled as vertically modular configurations following manufacturer specifications. To independently assess the effect of size versus geometric complexity, two designs, AR 5 (the largest real-world structure) and AR 6 (the smallest), were each modelled

at two scales. AR 5 was scaled down to match the spanwise length of AR6 (AR 5 Small), and AR 6 was scaled up to match AR 5's spanwise length (AR 6 Large). These scaled versions are not representative of real-world deployments but were created to decouple size from shape.

Three-dimensional mesh representations of each AR structure were obtained directly from manufacturers where available (AR 3, 6, 7) or were reconstructed from publicly available specification sheets or estimated from published photographs and news articles using computer-aided design software (AR 1, 2, 4). For ARs lacking detailed dimensional information, multiple images of each structure were collated and imported into ImageJ, where known dimensions of the structure, or reference objects visible within the images, were used to set the spatial scale, after which relevant structural metrics (height, width, feature sizes, feature angles) were measured (AR 5, 8). For finer-scale structural details, surface textures were reconstructed by digital sculpting either in Gravity Sketch or in Blender. Final assembly and construction of the three-dimensional meshes was completed in Blender and exported as OBJs. 3D meshes of the structures supplied by manufacturers, were provided with instructions not to distribute them, as a result AR 3, 6, and 7 will not be made publicly available, all others will be available at Kippax-Chui (2026).

Setup and execution of the Computational Fluid Dynamics simulation

The CFD domain dimensions were derived directly from the geometry of each artificial reef to ensure that every simulation provided a fair and consistent test of particle interception. The domain had to be large enough to allow the flow to develop naturally around the reef without artificial interference from the boundaries, while remaining computationally manageable. It was therefore scaled to the reef's streamwise length, spanwise width, and height, extending six times the streamwise length in the flow direction, five times the spanwise width laterally, and five times the height vertically. The reef itself was positioned 2.5 times its streamwise length downstream of the inlet and centred laterally within the domain, ensuring that the incoming flow was fully established before reaching it while leaving sufficient downstream distance for the wake to develop. The background mesh was generated with a base cell size of 0.16 m, determined through iterative sensitivity testing to balance computational cost against

resolution, with local refinement applied near the reef surface during meshing. The simulation runtime was set to allow the flow to clear the domain 3 times over, with a minimum of 400 seconds to ensure turbulent convergence in all cases. The full set of derived parameters and their calculation methods are provided in Appendix 1. The CFD simulations aim to model unidirectional static flow around submerged 3D AR geometries within a single-phase fluid domain representing seawater at 30°C. Static flow was used because the study's hypothesis concerns whether reef geometry alone influences particle collision probability. A steady, unidirectional current provides the conditions under which this relationship can be isolated, with geometry as the only variable changing between simulations. A flow velocity of 0.05 m s^{-1} was used, to match the mean back reef current speed recorded during coral mass spawning events across three Australian islands over a six year period (Hata et al., 2017). Here, the transient solver `pimpleFoam` was selected alongside the Reynolds-Averaged Navier-Stokes turbulence model k-ω SST (A. Rahman et al., 2020; Bordbar et al., 2025; OpenCFD Ltd, 2024) based on relevant literature investigating similar flow regimes, and openFOAM documentation. The k-ω SST model was selected as it provides a balance between computational efficiency and predictive accuracy by utilising two different equations for the free stream and for near wall behaviour (A. Rahman et al., 2020; ANSYS, Inc, 2024; Bordbar et al., 2025; Lin et al., 2025; SimScale, 2025; Yang et al., 2026).

Each structure was oriented at 0°, 45°, and 90° relative to the incoming flow direction (x axis) to assess the influence of deployment orientation on particle collision patterns. The 0° starting position of each AR corresponds to its most visually streamlined orientation, as shown in Figure 1, where the scale bars are aligned with the 0° streamwise direction. Structures that are rotationally symmetrical, i.e. the cube, sphere, AR 1, AR 5, and AR 5 Small were not simulated at 90°.

Simulation domains and boundary conditions were configured using the geometric and hydrodynamic parameters outlined in Appendix 1 and 2. Following case setup, the CFD domains were generated and meshed using the openFOAM pre-processing workflow, with the AR geometries embedded within the computational domain. During this embedding process the internal mesh of the fluid domain was iteratively refined 4 times as it approached the AR surface, refining from 16cm^3 cells to 1cm^3 cells. Between each level of refinement, a buffer of 10 cells was retained. This refinement allowed for higher resolution fluid movement to be resolved near the surface while avoiding phantom turbulence caused by sudden mesh

refinement in the fluid domain. Mesh quality and AR integration were assessed for visual aberrations in paraFOAM. AR mesh geometry and meshing parameters were iteratively refined prior to rerunning the meshing process to remove meshing artefacts that resulted in poor surface integration.

Simulations were run on the Imperial College HPC system (Harvey, 2017). The computational domain was decomposed into 20 parallel subdomains, efficiency testing showed that this level of decomposition allowed for faster processing time while utilising a low amount of resources, benefits to which are mostly seen on the internal queuing system. Post-processing functions were applied to extract cell centre coordinates across the domain, and the final 100 velocity timesteps, which represents 100 seconds of flow, as well as export the final AR surface mesh embedded within the CFD grid. Code, documentation, and an example case is available at Kippax-Chui (2026).

Setup and execution of the Particle Tracer simulation

The particle release parameters were tied to reef size to ensure a comparable particle supply across structures of very different dimensions. To achieve this, the release zone was scaled to each reef's cross-section, with particles introduced upstream across a plane that spanned twice the reef's spanwise width in the lateral direction and one and a half times its height in the vertical direction. The release plane was positioned just downstream of the inlet at a fixed streamwise coordinate of 0.1 m, with the vertical origin set at 0.02 m above the domain floor, and the lateral midpoint aligned with the reef's centre position. This configuration ensured that the release zone fully encompassed the reef's projected area while maintaining an equivalent particle concentration per unit cross-section across all simulations. A kill plane was placed 0.2 m upstream of the domain outlet to remove particles that had passed through the domain, preventing them from accumulating beyond the resolved flow field. The full set of derived parameters and their calculation methods are provided in Appendix 1.

Cell centre coordinates, the final 100 velocity timesteps from the CFD simulation, and the AR surface mesh extracted directly from the CFD domain were used to setup the particle simulation in CoRLSS. The CFD-derived mesh was used rather than the original geometry because modifications introduced during meshing altered local mesh resolution and simplified

some morphological features to ensure compatibility with the computational grid. Using the CFD-derived surface ensured consistency between the imported velocity field, mapped cell centres, and particle collision geometry. Near-surface mesh resolution was refined to approximately 1 cm around the AR surfaces, improving collision localisation accuracy, particularly for larger structures where the original meshes were comparatively sparse. Prior to import into CoRLSS, extracted meshes were cleaned in Blender and Meshlab to correct inverted normals and seal open boundaries generated during extraction from the CFD domain. After import, meshes were transformed to match Unity coordinate conventions within CoRLSS and assigned collision components to enable particle interaction with the AR surface.

Particles were released upstream of the AR from a rectangular release zone defined relative to the CFD domain dimensions. Exactly 1,000,000 particles were released per simulation with a fixed rate of five particles per frame and a particle tracking resolution of 50 frames per modelled time step. Since the CFD velocity field was output at 1 s intervals, this means each modelled time step is subdivided into 50 particle trajectory updates. The high temporal resolution ensures that every particle spends multiple sub steps within a given cell, allowing it to be influenced by that specific cell's velocity, both speed and direction, before passing into the next. To maintain physically realistic motion, the CFD velocities were divided by the number of frames per time step so that particles advanced by only the appropriate fraction of the full second displacement on each sub step. At the simulated flow speed of 0.05 m s^{-1}, the resulting displacement of ~1 mm per sub step is far smaller than the coarsest 16 cm background cells and an order of magnitude finer than the 1 cm near surface mesh, so particle motion is smoothly resolved throughout the domain and collisions are captured reliably. The spawning rate was chosen for computational efficiency, while the constant release area scaled to each structure's cross section yields a uniform volumetric particle concentration across all simulations. A downstream 'kill plane' positioned 0.2 m before the domain outlet removed particles exiting the active simulation region, preventing particle accumulation beyond the resolved flow field. Each particle simulation cycled through the 100 velocity timesteps until all particles had cleared the domain.

Particle radius was set to 0.0002 m based on measurements of the spanwise diameter of *Acropora kenti* larvae spawned at the Horniman Museum aquarium in January 2025. The spanwise diameter was selected rather than maximum body length because coral larvae are

oblong and generally swim with their longitudinal axis aligned to their direction of motion. It was therefore inferred that the spanwise plane represented the most likely region of interaction with settlement surfaces, as previous studies indicate larvae actively swim towards preferred settlement cues (Deshpande et al., 2025; Geertsma et al., 2023; Hata et al., 2017; Kundu et al., 2025; Reichert et al., 2025; Ricardo et al., 2017; Rippen et al., 2025).

Particle paths were determined using the imported CFD flow velocity data, with particle movement calculated between neighbouring cell centres throughout the domain. The coordinates of particle collisions with the AR surface, along with the pre-collision trajectories of colliding particles, were recorded and exported as log files for subsequent analyses.

Structure-Scale Complexity Quantification and Statistical Analysis

To capture the size, overall shape, and surface texture of each artificial reef at the whole-structure scale, a set of geometric and informational descriptors was calculated from the processed 3D meshes. The metrics fall into three categories: (1) size-related measures: surface area, mesh volume, convex hull area, convex hull volume, aspect ratio, and axis-aligned bounding box (AABB) volume; (2) surface-complexity measures: convexity ratio (mesh volume divided by convex hull volume), packing (the proportional difference between mesh surface area and convex hull surface area, capturing surface indentation and internal voids), and fractal dimension (estimated via a voxel-based box-counting method in `trimesh`); and (3) informational complexity measures calculated following Riera et al (2024). For informational complexity, face normals were converted to spherical coordinates and binned into a two-dimensional angular histogram, from which orientation richness, diversity, and evenness were derived using occupancy and Shannon entropy-based metrics.

For each AR and flow angle, the total number of particle collisions recorded in the Lagrangian simulations was paired with the structure-scale geometric metrics, yielding a single combined dataset for statistical analysis. The level of correlation between each structure-level geometric metric and collision percentage was assessed using Spearman’s rank

correlation coefficients (ρ). This non-parametric test was selected for its robustness to non-normal distributions, outliers, and non-linear monotonic trends.

To account for the repeated-measures of each AR across the three flow angles (0°, 45°, and 90°), a Generalised Estimating Equations (GEE) model with an exchangeable working correlation structure was employed (Hilbe, 2016; Liang and Zeger, 1986). Because collision outcomes are binary, a binomial error distribution with a logit link was specified. Many of the structure-scale complexity metrics were highly collinear, therefore Variance Inflation Factor (VIF) screening was applied to select a set of uncorrelated predictors (O'brien, 2007), which retained flow angle, frontal area, and packing as the representative variables for orientation, size, and surface complexity, respectively. Robust standard errors were used to ensure valid inference despite the large between-reef heterogeneity in collision counts. Results are reported as odds ratios (OR), where values less than 1 indicate lower odds of collision and values greater than 1 indicate higher odds of collision, relative to the reference category or per-unit increase in the predictor. The custom scripts that perform these analyses are provided in Kippax-Chui (2026).

Vertex-Scale Complexity Quantification and Statistical Analysis

To identify the local surface features that most strongly promote particle interception, five geometric descriptors were computed for every vertex of each AR mesh. These descriptors were chosen to capture the orientation, curvature, and spatial context that a passively transported larva would encounter in the final centimetres of its approach: Figure 2 a) surface slope (steepness relative to the seabed), b) flow facing angle (orientation relative to the incident current), c) relative curvature (a dimensionless measure of local surface irregularity), d) signed curvature in degrees (to distinguish convex from concave features), and e) distance to high curvature regions (proximity to the most geometrically complex parts of the reef). Together, these features capture whether a surface is facing the flow, how sharply it protrudes or recedes, and whether it lies within the immediate hydrodynamic influence of a prominent edge or bump. This approach enables the direct association of local surface geometry with collision likelihood, bypassing the averaging inherent in structure scale metrics.

The five geometric descriptors were then calculated per vertex. Surface slope was calculated as the angle between the vertex normal vector and the vertical axis, expressed in degrees, with 0° being up and 180° being down. Flow-facing angle was calculated as the angle between the vertex normal vector and the incident flow direction, expressed in degrees. To calculate curvature in degrees, a custom signed curvature metric was devised to directly capture the convex or concave nature of surface features. For each vertex, the angle between its normal and each incident face normal was computed. The sign was set positive when the face centroid lay behind the vertex normal (convex outward) and negative otherwise (concave inward). The per-vertex curvature was defined as the mean of these signed angles over all incident faces. Values are reported in degrees. Relative curvature, a dimensionless curvature metric, was estimated using principal component analysis of 50 neighbouring vertices identified using a k-nearest-neighbour search (Pauly et al., 2003), here 30 neighbours were found to produce similar patterns as curvature in degrees. Curvature was defined as the ratio between the smallest eigenvalue and the sum of eigenvalues derived from the local covariance matrix, with larger values indicating greater local geometric irregularity. Using this relative curvature metric, distance to high-curvature regions was calculated as the Euclidean distance from each vertex to the nearest vertex exceeding a defined curvature threshold. Here the threshold was set to 0.04, determined via a visual inspection of the curvature scalar projected on to the ARs.

To examine how collision probability varied with each geometric measure, vertices were binned into fixed-width intervals for each descriptor. A bias-corrected collision probability was then calculated for each bin by dividing the total number of collisions in the bin by the number of vertices it contained. This correction prevents mesh regions that are heavily represented (such as large flat areas) from dominating the signal, ensuring that the collision patterns reflect genuine geometric associations rather than uneven vertex sampling.

Spearman's ρ was similarly employed to evaluate the monotonic relationships between local geometric features and per-vertex collision counts, providing a robust measure of association without assuming bivariate normality or a specific functional form. To formally test associations between vertex-level geometric metrics and collision counts while accounting for the repeated measures (multiple flow angles per reef), Poisson GEE models were used,

following the framework of Liang and Zeger (1986). Each model included a single geometric predictor, together with flow angle as a categorical covariate. An independence working correlation structure was specified, with AR structure as the clustering variable to accommodate within-reef correlation, robust standard errors were employed for inference. For the three curvature-related features: relative curvature, signed curvature, and distance to high-curvature regions, binned probability plots suggested possible non-monotonic relationships. A quadratic term was therefore added to each of those models, and the linear and quadratic coefficients were tested independently, in order to determine if the suspected non-monotonic trend followed a linear or quadratic form. Results are reported as rate ratios (RR) from linear Poisson models, which quantify the relative change in the expected collision count per vertex. An RR below 1 signifies a reduction in collision rate, while an RR above 1 signifies an increase. For the quadratic models, results are reported as β coefficients for the linear and quadratic terms. The linear coefficient describes the initial direction of the association, while the quadratic coefficient describes the curvature, together they indicate whether the relationship accelerates, decelerates, or changes direction. The analyses are provided in Kippax-Chui (2026).

Results

Influence of Flow angle on collision patterns

Figure 3 shows the percentage of released particles that collided with each artificial reef at each simulated flow angle. Because the particle-release area was scaled to the cross-section of each reef and the spawning rate was held constant, the particle concentration was identical across all simulations. The most angle-sensitive structures were AR3b and AR8 (Figure 3), both of which reached their highest collision rates at 45° and showed the greatest within-design variation across orientations, with collision percentages increasing by 1.5 times between the best and worst angles. AR6 on the other hand showed higher-than-average variation at 0°.

For most of the size-related metrics (Figure 4a–f), intra-structure variation between the three flow angles was generally modest. As a result of the axis-dependent calculation method for frontal area (Figure 4a) and AABB volume (Figure 4f), a small angle-to-angle scatter is observed, but the shifts were minor for the majority of reefs.

This angle-specific sensitivity was further quantified in the structure-scale GEE model. Relative to 0°, a 45° incidence did not significantly alter collision odds. However, structures oriented at 90° had significantly reduced collision odds relative to 0° (OR = 0.82), supporting the trends observed in Figure 2 and 3.

Influence of structure size on collision patterns

AR6 achieved the highest overall collision rate at 3.2 % at 0° (Figure 3), and its 45° and 90° orientations were also among the top-performing cases (2.5 % and 2.1 %, respectively). Critically, when AR6 was scaled up (AR6 Big) to match the spanwise length of the largest structure (AR5), collision rates fell sharply by roughly 65 % at 0°, 77 % at 45°, and 58 % at 90°. The reverse scaling experiment yielded inverted results, where AR5 Small intercepted roughly twice the percentage of particles as its full-sized counterpart AR5.

Beyond these scaling experiments, Figure 4 revealed a consistent pattern across all metrics that capture overall size: a) frontal area, b) footprint area, c) volume, d) convex hull area, e) convex hull volume, and f) AABB volume all showed a broadly negative relationship with collision percentage. Structures with larger values of these metrics tended to produce lower collision rates, irrespective of flow angle. This uniform direction of effect is reinforced by the Spearman rank correlations in Figure 5a, where every size-related metric exhibited a negative ρ coefficient. The statistical models confirmed this size-driven effect. Greater frontal area was significantly associated with lower collision odds (OR = 0.73 per m^2).

Influence of structural complexities on collision patterns

Unlike the size metrics, complexity-related metrics across Figure 4, including g) packing, i) fractal dimension, k) orientation diversity, and l) orientation evenness, showed a positive

trend, with positive Spearman ρ coefficients in Figure 5a, though only fractal dimension showed a statistically significant relationship. The GEE model reinforces this: higher packing significantly increases collision odds (OR = 1.13 per unit). Aspect ratio, a dimensionless elongation metric that changes with angle, owing to the axis-dependent calculation method, exhibited a similarly positive visual relationship with collision percentage in Figure 4m, supported by a weak positive Spearman ρ in Figure 5a, though this relationship was not statistically significant. Similarly, orientation richness (Figure 4j and Figure 5a) a non-significant weak negative relationship with collision percentage.

Influence of Vertex-scale complexities on collision patterns

Vertex-scale complexity metrics showed generally weaker associations with collision probability than the structure-scale metrics (Figure 5b). Slope exhibited no discernible relationship, while weak negative associations were observed for flow-facing angle and distance to high-curvature features, and weak positive associations were seen for relative and signed curvature. Similar trends are visible across Figure 6, although for relative and signed curvature the relationships is non-monotonic. Relative curvature peaks at approximately 0.13 (Figure 6c) and signed curvature peaks roughly between 54° and 66° (Figure 6e).

In Figures 6c-e, results shown in grey should be interpreted with caution as their normalised probabilities have low signal to noise ratios and are disproportionately influenced by random sampling variation as they contain very few vertices and very few collisions. After bias correction, distance to high-curvature features remained the only vertex-scale metric that maintained a high collision probability in bins containing a relatively large number of vertices, specifically in the bin approximately 0–2 cm from high-curvature vertices (Figure 6d). At a much lower probability, a secondary peak also appeared roughly 40–42 cm from high-curvature vertices. Flow-facing angle (Figure 6b) displayed a broadly negative trend after normalisation, yet the highest collision probability occurred when the vertex normal was oriented between 6° and 12° of the incident flow direction.

In the Poisson GEE models with linear terms, vertex flow-facing angle showed a strong negative association with per-vertex collision count (rate ratio = 0.39). Signed curvature showed a positive association (rate ratio = 1.60). Distance to high-curvature regions was

negatively associated (rate ratio = 0.20). Vertex slope and relative curvature were not significant in the linear models.

Because binned visualisations suggested non-monotonic patterns for the curvature-related features, quadratic terms were added as secondary analyses. For relative curvature, both the linear ($\beta = 1.43$) and quadratic ($\beta = -0.66$) terms were significant, indicating a concave-down relationship, where collision count increased with curvature but the rate of increase diminished at higher values. The fitted peak lay beyond the observed curvature range (≈1.08), a consequence of the parabolic model smoothing over the local dip and secondary peak visible in the binned plot (Figure 5c). A simple parabola cannot reproduce a high-low-high pattern, the binned distribution provides a more reliable picture of the detailed shape. For signed curvature, the quadratic term was not significant, supporting the simpler linear positive relationship. For distance to high-curvature features, the binned distribution was bimodal and could not be captured by a quadratic model, the linear negative trend was therefore retained as the primary summary.

Discussion

At the structure scale, flow angle was identified as a categorical factor that significantly influenced collision count, particularly at 90°, where the odds of a particle striking the reef were reduced by roughly one-fifth relative to the 0° direction. This directional sensitivity likely arises from the way the artificial reefs were oriented in the simulations, because the structures had no designated front or back and were not designed to be hydrodynamic in a particular direction, in the initial alignment the ARs were placed with the longest dimension of each reef parallel to the incident flow at 0°. As a result, rotating an AR to 90° always presented the broadest face of the reef to the incoming flow, thereby increasing its frontal area.

After screening for collinearity, frontal area (projected area (m^2) of the reef perpendicular to the incident flow) was chosen as the primary descriptor for overall size of the ARs. From the dataset analysed, per m^2 increase in frontal area resulted in 27% decrease in collision likelihood. While it may be intuitively assumed that larger structures will cover a greater area

and hence intercept more particles, size was controlled for in this study in order to isolate specific design elements across the ARs to better understand which features may be more conducive for larval settlement. As the area over which the particles are released is scaled to the size of the structure and the total number of particles released is identical for all structures, a drop in collision likelihood in these experiments would translate into a decrease in larvae collision efficiency. This effect is likely due to the deflective effect on flow, that having a larger surface area causes (Jiao et al., 2017). This effect is often designed intentionally for in ARs used to support fish populations, as it leads to areas of upwelling and low flow and support resuspension of particulate organic matter that are beneficial for juvenile fish population (Jiang et al., 2016; Leftheriotis et al., 2025; Liu et al., 2013; Maslov et al., 2023). For passive larval delivery, however, the same mechanism becomes a hindrance and may represent a design trade-off. Flow deflection is less desirable during settlement, yet its potential effect on filter feeding once corals have become established on the structure remains unexplored. The size-scaling experiments emphasises the effect of size, as when the geometry of the smallest (AR 6) was enlarged to match the span of the largest (AR 6 Big), its collision rate dropped by more than half, while the scaled-down version of the largest reef (AR 5 Small) captured approximately double the proportion of particles of its full-sized parent. Thus, while a large frontal area may serve other restoration goals, it systematically reduces the passive interception of coral larvae by deflecting them away from the reef surface.

While frontal area is the dominant size-related control, structural complexity independently enhances particle interception. Here complexity is captured through packing, a metric that quantifies how much a reef's surface deviates from a smooth convex envelope, with higher values indicating more indentations, crevices, and internal voids. Across the full dataset, reefs with greater packing consistently achieved higher collision rates, even when frontal area was comparable. For instance, AR 1 and the reference cube share nearly identical external dimensions and frontal area (Figure 1, Figure 4 a, b, d, e, f), yet AR 1, with its heavily textured and perforated surface, intercepted over four times more particles. The most plausible explanation is hydrodynamic. Irregular surfaces disrupt the prevailing flow, thickening the slow-moving boundary layer near the reef and creating a zone of reduced velocity where passively drifting particles are more likely to make contact rather than being swept past (Hata et al., 2017; Lanham et al., 2025; Levenstein et al., 2022; Reichert et al., 2025). Such low-flow micro-habitats are well-known in fishery and coastal defence-oriented

reefs, where crevices shelter juvenile fish and dissipate wave energy (Jiao et al., 2017; Kim et al., 2014; Leftheriotis et al., 2025; Liu and Su, 2013; Santiago Caamaño et al., 2022; Vivier et al., 2021; Woo et al., 2014; Xia et al., 2024; Zhang et al., 2021; Zhou et al., 2022). For larval delivery, the same principle has been demonstrated at much finer, millimetre scales (Hata et al., 2017; Lanham et al., 2025; Reichert et al., 2025), where surface complexity not only increases recruitment of live larvae but also improves post-settlement survivorship (Reichert et al., 2025). Our findings suggest that deliberately designing for high packing, by incorporating indentations and convolutions, offers an effective, geometry-based strategy for boosting passive larval interception, independent of overall reef size.

Packing does not, however, fully explain all the patterns in the data. Several structures achieved high collision counts despite low packing values, pointing to additional geometric mechanisms. AR 4, for example, has a wireframe construction that yields an exceptionally low packing score, yet its open lattice allows flow to pass through while its many edges and intersections still intercept particles effectively. AR 3a, whose surface area closely matches its convex hull, likewise sustained high collisions at all angles. AR 8 exhibited the strongest orientation sensitivity in the dataset, with collision rates rising sharply at 45° and falling again at 90°, despite relatively stable packing values. In these cases, local flow effects generated by protruding elements, open frameworks, or orientation-specific turbulence appear to override the global packing signal. These exceptions highlight that while packing is a useful overall proxy for surface complexity, certain geometric configurations can promote interception through mechanisms not captured by the convex-hull-based metric alone, and future design screening may benefit from a small suite of complementary descriptors.

Analysis of vertex-scale descriptors sheds light on the effects of specific geometrical features. Slope, the orientation of a surface relative to the seabed, showed no detectable influence on collision probability (Figure 6a), indicating that verticality alone does not inherently promote or hinder particle interception. In contrast, surfaces that faced more directly into the incident flow consistently experienced higher collision counts. Notably, collision probability did not peak at exactly head-on but at a slight offset of approximately 2–4° from the flow direction (Figure 6b). This may reflect a similar deflective mechanism to that observed for frontal area at the whole-structure scale, where a surface that directly confronts the flow can deflect oncoming particles away abruptly, whereas a slightly angled surface steers the flow along its

face, carrying particles further downstream and increasing the likelihood that they contact the reef further along. Because most surface normals across the reef meshes were only gently inclined relative to the incoming current, rather than sharply perpendicular, particles would frequently have been redirected along these shallow-angled surfaces instead of being bounced away immediately. This gentle steering promotes sustained near-surface transport and, ultimately, settlement rather than deflection. By linking collision patterns to these vertex-level geometric traits, we can move beyond bulk complexity metrics and begin to specify the precise surface configurations that enhance interception.

These collision patterns relative to both curvature metrics suggest that gentle, outward bulging features are particularly effective at intercepting particles. The likely explanation lies in local flow dynamics. Convex protrusions tend to diverge the approaching flow, allowing fluid and the particles entrained within it to maintain their inertia and continue toward the surface, whereas concave indentations converge the flow, potentially accelerating it and carrying particles away from the reef before they can settle (Gan et al., 2024; Peren et al., 2015). This interplay is clearly visible on AR 7 Brick at 90°, where collision hotspots concentrate on convex undulations and cylindrical protrusions, slightly offset from the most directly flow facing surfaces, consistent with the 2–4° angular offset discussed earlier (Figure 7a). Although the bulk flow largely diverges around the entire reef at this orientation (Figure 7b), the local flow direction near the surface still aligns with the collision locations, indicating that particles are steered onto the convex features even as the main current passes around the structure. However, a structure composed exclusively of convex features, such as the sphere, or one dominated by flat and convex planes, like the cube, both recorded among the lowest collision counts in the dataset. This indicates that while convex curvature boosts interception at the local scale, concave recesses and surface indentations remain essential to provide the overall complexity that traps and retains particles, as seen with packing, and to prevent the excessive flow deflection that occurs when a reef is too streamlined or too large.

Distance to high-curvature regions showed a strong negative association with collision probability, with the vast majority of collisions concentrated within the first 0–2.5 cm of a curved feature before falling off sharply (Figure 6d). This immediate spatial clustering reinforces the earlier finding that both signed and relative curvature were strong predictors of interception. The tight concentration of impacts directly on or very near curved vertices

confirms that these features act as reliable, high-signal collision hotspots. The strong drop-off with distance suggests that the hydrodynamic influence of a curved feature, likely boundary-layer disruption and local flow deceleration, is felt only over a short range, beyond which the collision rate returns to background. A secondary peak in collision probability, visible at approximately 40 cm from curved features, may reflect the same deflective mechanism described earlier, in which convex features redirect flow and entrained particles onto downstream surfaces, creating a second, more diffuse zone of enhanced interception. Together, these patterns indicate that the collision-enhancing effect of curvature is strongest within the immediate hydrodynamic footprint of a curved feature but can also propagate further downstream with reduced intensity.

By intentionally setting aside flow variability and larval behaviour, this study isolated how reef geometry itself brings particles into contact with the surface. The results show that geometry is not a passive backdrop. At the whole-reef scale, larger frontal area deflects flow and lowers collision odds, while higher surface packing traps particles by creating slow-moving boundary layers. At the centimetre scale, convex curvature and a slight flow-facing angle further concentrate collisions. These effects involve clear trade-offs. A design that increases packing can also shield the very convex features that best capture particles, and an asymmetrical AR oriented to minimise frontal area at one flow angle may present a much wider, deflection-prone face when the current shifts. Because natural flow direction varies with tides, waves, and storms, a single fixed orientation cannot perform optimally all the time.

Two further considerations add depth to this design picture. First, corals that recruit and grow on the structures will themselves modify the local flow field. Depending on growth form, how may colonies channel water toward themselves to enhance filter feeding or deflect flow away to reduce competition, slowly reshaping the hydrodynamic landscape over time. Similarly, how may the same influences on flow affect the accumulation of sediment. The optimal starting geometry is therefore only the first step in a dynamic process, and the collision patterns we report may shift as the biological community develops. Second, when multiple reefs are deployed together, the wakes and flow deflections of upstream units will alter the delivery of larvae to those downstream. While array configurations have been studied for their ability to create larger low flow refuges for fish (Androulakis et al., 2020;

Liu and Su, 2013; Xia et al., 2024; Zhou et al., 2022), their effect on larval interception, food delivery, and sediment accumulation have not been explored. Depending on spacing and geometry, an array could either steer larvae toward settlement favourable surfaces or inadvertently deflect them away. Are a homogenous or heterogeneous set of designs, more suitable to maintain interception across a wider range of flow directions? The quantitative relationships developed here between size, packing, curvature, and collision probability offer a foundation for weighing these considerations, moving restoration from a fixed geometric blueprint toward a more flexible, ecologically responsive design approach.

Conclusions

To make coral restoration more scalable, particularly on reefs damaged by coastal development, artificial reefs must be designed to promote natural larval settlement. This study shows that reef geometry strongly controls the probability of passive particle collisions, the essential precursor to active settlement. At the whole-structure scale, reefs with smaller frontal areas consistently intercepted a greater proportion of particles, while higher surface packing, reflecting more indentations and voids, further boosted collision likelihood. At the centimetre scale, convex-curved surfaces acted as local capture hotspots, but only when they formed part of an otherwise complex, indented structure, purely convex shapes like a smooth sphere performed poorly. Importantly, these broad geometric trends could be overridden by specific structural details, such as open lattice frameworks or perforations, demonstrating that per-structure CFD simulation remains the most reliable way to evaluate a given design. The open-source computational framework we provide offers a direct route to such evaluations, while the geometric relationships identified here, linking smaller size, higher packing, and convex curvature within complex surfaces to greater particle interception, can serve as practical shortcuts for initial screening. Together, these results reveal a systematic trade-off between flow deflection and surface trapping, moving restoration practice toward a predictive, geometry-informed design paradigm.

Funding

Oliver Kippax-Chui was funded by the NERC Science and Solutions for a Changing Planet Doctoral Training Programme (grant number NE/S007415/1).

Declaration of competing interest

The authors declare that they have no known competing financial interests or personal relationships that could have appeared to influence the work reported in this paper.

References

A. Rahman, M.A., Nazri, M.N., Fitriadhy, A., Ahmad, M.F., Kasiman, E.H., Musa, M.A., Alias, F., Mohd, M.H., 2020. A Fundamental CFD Investigation of Offshore Structures for Artificial Coral Reef Development. CFDL 12, 110–125. https://doi.org/10.37934/cfdl.12.7.110125

Androulakis, D., Dounas, C., Banks, A., Magoulas, A., Margaris, D., 2020. An Assessment of Computational Fluid Dynamics as a Tool to Aid the Design of the HCMR-Artificial-ReefsTM Diving Oasis in the Underwater Biotechnological Park of Crete. Sustainability 12, 4847. https://doi.org/10.3390/su12124847

ANSYS, Inc, 2024. Shear-Stress Transport (SST) k-ω Model.

Bao, D.W., Yu, J., Luo, D., 2026. Integrating computational fluid dynamics and topological optimization for generative design of artificial reefs. ARIN 5, 4. https://doi.org/10.1007/s44223-025-00109-z

Blender Online Community, 2018. Blender - a 3D modelling and rendering package.

Bordbar, A., Knir, J., Kelefouras, V., Hickling, S.J.S., Short, H., Lee, Y.C., 2025. Flow Dynamics and Local Scour Around Seabed-Mounted Artificial Reefs: A Case Study from Torbay, UK. JMSE 13, 1425. https://doi.org/10.3390/jmse13081425

Boström-Einarsson, L., Babcock, R.C., Bayraktarov, E., Ceccarelli, D., Cook, N., Ferse, S.C.A., Hancock, B., Harrison, P., Hein, M., Shaver, E., Smith, A., Suggett, D., Stewart-Sinclair, P.J., Vardi, T., McLeod, I.M., 2020. Coral restoration – A systematic review of current methods, successes, failures and future directions. PLoS ONE 15, e0226631. https://doi.org/10.1371/journal.pone.0226631

Carral, L., Lamas, M.I., Cartelle Barros, J.J., López, I., Carballo, R., 2022. Proposed Conceptual Framework to Design Artificial Reefs Based on Particular Ecosystem Ecology Traits. Biology 11, 680. https://doi.org/10.3390/biology11050680

Cignoni, P., Callieri, M., Corsini, M., Dellepiane, M., Ganovelli, F., Ranzuglia, G., 2008. MeshLab: an Open-Source Mesh Processing Tool.

Deshpande, K., Gysbers, D., Yus, J., Van Bendegom, D., Nixon, E., McClintock, R., Quinlan, Z.A., Marhaver, K.L., Kelly, L.W., Espinosa-Marzal, R.M., Johnson, A.J.W., Juarez, G., 2025. Direct observation and quantitative characterization of chemotactic behaviors in Caribbean coral larvae exposed to organic and inorganic settlement cues. Sci Rep 15, 10173. https://doi.org/10.1038/s41598-025-93194-z

735 Düzbastılar, F.O., Şentürk, U., 2009. Determining the weights of two types of artificial reefs
736 required to resist wave action in different water depths and bottom slopes. Ocean
737 Engineering 36, 900–913. https://doi.org/10.1016/j.oceaneng.2009.06.008
738 Fiji, n.d.
739 Galdo, M.I.L., Guerreiro, M.J.R., Vigo, J.L., Rodriguez, I.A., Lorenzo, R.V., Couce, J.C.C.,
740 Couce, L.C., 2022. Definition of an Artificial Reef Unit through Hydrodynamic and
741 Structural (CFD and FEM) Models—Application to the Ares-Betanzos Estuary.
742 JMSE 10, 230. https://doi.org/10.3390/jmse10020230
743 Gan, W., Guo, H., Zhang, H., Zhao, F., Li, J., Peng, S., He, Y., 2024. Wind-Driven Dynamics
744 Around Building Clusters: Impact of Convex and Concave Curvilinear Morphologies
745 and Central Angles. Atmosphere 15, 1454. https://doi.org/10.3390/atmos15121454
746 Geertsma, R.C., Kamermans, P., Murk, A.J., Wijgerde, T., 2023. Real-time high resolution
747 tracking of coral and oyster larvae. Journal of Experimental Marine Biology and
748 Ecology 565, 151910. https://doi.org/10.1016/j.jembe.2023.151910
749 Gravity Sketch, n.d.
750 Hansen, C.D., Johnson, C.R., 2005. The visualization handbook. Elsevier-Butterworth
751 Heinemann, Amsterdam Boston.
752 Harvey, M., 2017. Imperial College Research Computing Service.
753 https://doi.org/10.14469/HPC/2232
754 Hata, T., Madin, J.S., Cumbo, V.R., Denny, M., Figueiredo, J., Harii, S., Thomas, C.J., Baird,
755 A.H., 2017. Coral larvae are poor swimmers and require fine-scale reef structure to
756 settle. Sci Rep 7, 2249. https://doi.org/10.1038/s41598-017-02402-y
757 Higgins, E., Metaxas, A., Scheibling, R.E., 2022. A systematic review of artificial reefs as
758 platforms for coral reef research and conservation. PLoS ONE 17, e0261964.
759 https://doi.org/10.1371/journal.pone.0261964
760 Hilbe, J.M., 2016. Practical Guide to Logistic Regression. CRC Press, Boca Raton.
761 Huang, J., Li, J., Li, Y., Gong, P., Guan, C., Xia, X., 2024. Flow Field Characteristics of
762 Multi-Trophic Artificial Reef Based on Computation Fluid Dynamics. J. Ocean Univ.
763 China 23, 317–327. https://doi.org/10.1007/s11802-024-5559-3
764 Hughes, T.P., Baird, A.H., Morrison, T.H., Torda, G., 2023. Principles for coral reef
765 restoration in the anthropocene. One Earth 6, 656–665.
766 https://doi.org/10.1016/j.oneear.2023.04.008

767 Jiang, Z., Liang, Z., Zhu, L., Liu, Y., 2016. Numerical simulation of effect of guide plate on
768 flow field of artificial reef. Ocean Engineering 116, 236–241.
769 https://doi.org/10.1016/j.oceaneng.2016.03.005
770 Jiao, L., Yan-xuan, Z., Pi-hai, G., Chang-tao, G., 2017. Numerical simulation and PIV
771 experimental study of the effect of flow fields around tube artificial reefs. Ocean
772 Engineering 134, 96–104. https://doi.org/10.1016/j.oceaneng.2017.02.016
773 Kim, D., Jeong, J.-Y., Jung, S., Na, W.-B., 2024. Evaluating the particulate organic matter
774 particles distribution characteristics around artificial reefs using computational fluid
775 dynamics. Ocean Engineering 292, 116574.
776 https://doi.org/10.1016/j.oceaneng.2023.116574
777 Kim, D., Woo, J., Yoon, H.-S., Na, W.-B., 2014. Wake lengths and structural responses of
778 Korean general artificial reefs. Ocean Engineering 92, 83–91.
779 https://doi.org/10.1016/j.oceaneng.2014.09.040
780 Kippax-Chui, O., 2026. CFD Informed Particle Collision Modelling.
781 https://doi.org/10.5281/ZENODO.23369375
782 Kundu, S., Potenti, S., Quinlan, Z.A., Willard, H., Chen, J., Noritake, T., Levy, N., Karimi,
783 Z., Jorissen, H., Hancock, J.R., Drury, C., Kelly, L.W., De Cola, L., Chen, S.,
784 Wangpraseurt, D., 2025. Biomimetic chemical microhabitats enhance coral
785 settlement. Trends in Biotechnology 43, 2232–2250.
786 https://doi.org/10.1016/j.tibtech.2025.03.019
787 Lanham, B.S., Pomeroy, A.W.M., Swearer, S.E., Marusic, I., Javaherchian, J., Morris, R.L.,
788 2025. Substrate-mediated alterations to hydrodynamic conditions enhances shellfish
789 larval settlement: Implications for artificial reef restoration. Ecological Engineering
790 212, 107474. https://doi.org/10.1016/j.ecoleng.2024.107474
791 Leftheriotis, G.A., Sibetheros, I.A., Dimas, A.A., 2025. Large-eddy simulation of the
792 turbulent oscillatory flow around an artificial reef. Ocean Engineering 318, 120142.
793 https://doi.org/10.1016/j.oceaneng.2024.120142
794 Lenton, T. M., Milkoreit, M., Willcock, S., Abrams, J. F., Armstrong McKay, D. I., Buxton,
795 J. E., Donges, J. F., Loriani, S., Wunderling, N., Alkemade, F., Barrett, M.,
796 Constantino, S., Powell, T., Smith, S. R., Boulton, C. A., Pinho, P., Dijkstra, H. A.,
797 Pearce-Kelly, P., Roman-Cuesta, R. M., Dennis, D., 2025. The Global Tipping Point
798 Report 2025. University of Exeter.
799 Levenstein, M.A., Gysbers, D.J., Marhaver, K.L., Kattom, S., Tichy, L., Quinlan, Z., Tholen,
800 H.M., Wegley Kelly, L., Vermeij, M.J.A., Wagoner Johnson, A.J., Juarez, G., 2022.

Millimeter-scale topography facilitates coral larval settlement in wave-driven oscillatory flow. PLoS ONE 17, e0274088. https://doi.org/10.1371/journal.pone.0274088

Li, Z., Zheng, Y., Lv, S., Xie, W., Zhu, L., Wang, L., Ma, J., Guo, C., Zhang, Y., Liang, Z., Jiang, Z., 2025. Hydrodynamic performance of artificial reef with guide plates: A combined computational fluid dynamics and particle image velocimetry investigation. Applied Ocean Research 165, 104865. https://doi.org/10.1016/j.apor.2025.104865

Liang, K.-Y., Zeger, S.L., 1986. Longitudinal data analysis using generalized linear models. Biometrika 73, 13–22. https://doi.org/10.1093/biomet/73.1.13

Limer, B.D., Payne, O., Brancato, A., Mitchell, M., Abu-Kubie, C., Figueiredo, J., Holstein, D.M., 2024. Life history and early ontogeny determine vertical swimming behaviors in the larvae of Caribbean corals. Journal of Experimental Marine Biology and Ecology 578, 152035. https://doi.org/10.1016/j.jembe.2024.152035

Lin, X., Wang, Q., Yu, X., Li, Q., 2025. Effect of submerged depth on the flow field around different artificial reefs. Physics of Fluids 37, 083114. https://doi.org/10.1063/5.0282515

Liu, T.-L., Su, D.-T., 2013. Numerical analysis of the influence of reef arrangements on artificial reef flow fields. Ocean Engineering 74, 81–89. https://doi.org/10.1016/j.oceaneng.2013.09.006

Liu, Y., Zhao, Y., Dong, G., Guan, C., Cui, Y., Xu, T.-J., 2013. A study of the flow field characteristics around star-shaped artificial reefs. Journal of Fluids and Structures 39, 27–40. https://doi.org/10.1016/j.jfluidstructs.2013.02.018

Maslov, D., Pereira, E., Duarte, D., Miranda, T., Ferreira, V., Tieppo, M., Cruz, F., Johnson, J., 2023. Numerical analysis of the flow field and cross section design implications in a multifunctional artificial reef. Ocean Engineering 272, 113817. https://doi.org/10.1016/j.oceaneng.2023.113817

Norris, B.K., Reguero, B.G., Bartolai, J., Yukish, M.A., Rhode-Barbarigos, L., Haus, B.K., Ojeda, G.B., Maza, M., Lara, J.L., Beck, M.W., 2025. Designing modular, artificial reefs for both coastal defense and coral restoration. Coastal Engineering 199, 104742. https://doi.org/10.1016/j.coastaleng.2025.104742

O'brien, R.M., 2007. A Caution Regarding Rules of Thumb for Variance Inflation Factors. Qual Quant 41, 673–690. https://doi.org/10.1007/s11135-006-9018-6

OpenCFD Ltd, 2024. k-ω Shear Stress Transport (SST).

834 Pauly, M., Keiser, R., Gross, M., 2003. Multi-scale Feature Extraction on Point-Sampled
835 Surfaces. Computer Graphics Forum 22, 281–289. https://doi.org/10.1111/1467-
836 8659.00675
837 Peren, J.I., Van Hooff, T., Ramponi, R., Blocken, B., Leite, B.C.C., 2015. Impact of roof
838 geometry of an isolated leeward sawtooth roof building on cross-ventilation: Straight,
839 concave, hybrid or convex? Journal of Wind Engineering and Industrial
840 Aerodynamics 145, 102–114. https://doi.org/10.1016/j.jweia.2015.05.014
841 Perkol-Finkel, S., Zilman, G., Sella, I., Miloh, T., Benayahu, Y., 2008. Floating and fixed
842 artificial habitats: Spatial and temporal patterns of benthic communities in a coral reef
843 environment. Estuarine, Coastal and Shelf Science 77, 491–500.
844 https://doi.org/10.1016/j.ecss.2007.10.005
845 Perricone, V., Mutalipassi, M., Mele, A., Buono, M., Vicinanza, D., Contestabile, P., 2023.
846 Nature-based and bioinspired solutions for coastal protection: an overview among key
847 ecosystems and a promising pathway for new functional and sustainable designs.
848 ICES Journal of Marine Science 80, 1218–1239.
849 https://doi.org/10.1093/icesjms/fsad080
850 Reichert, J., Jorissen, H., Drury, C., Hancock, J.R., Haynes, C., Nims, A.D., Rova, L.H.,
851 Schiettekatte, N.M.D., Madin, J.S., 2025. Helix recesses boost coral larvae settlement
852 and survival. Biological Conservation 311, 111407.
853 https://doi.org/10.1016/j.biocon.2025.111407
854 Ricardo, G.F., Jones, R.J., Nordborg, M., Negri, A.P., 2017. Settlement patterns of the coral
855 Acropora millepora on sediment-laden surfaces. Science of The Total Environment
856 609, 277–288. https://doi.org/10.1016/j.scitotenv.2017.07.153
857 Riera, E., Hubas, C., Ungermann, M., Rigot, G., Pey, A., Francour, P., Rossi, F., 2023.
858 Artificial reef effectiveness changes among types as revealed by underwater
859 hyperspectral imagery. Restoration Ecology 31, e13978.
860 https://doi.org/10.1111/rec.13978
861 Riera, E., Mauroy, B., Francour, P., Hubas, C., 2024. Establishing complexity targets to
862 enhance artificial reef designs. Sci Rep 14, 22060. https://doi.org/10.1038/s41598-
863 024-72227-z
864 Rippen, J.C., Wijers, T., Van Bruggen, C.G.E., Antoun, M., Eriksson, B.K., Hylkema, A.,
865 2025. Material matters: artificial substrate composition and biofilm presence
866 influence larval settlement of Diadema antillarum. Front. Mar. Sci. 12, 1596378.
867 https://doi.org/10.3389/fmars.2025.1596378

Santiago Caamaño, L., Lamas Galdo, M.I., Carballo, R., López, I., Cartelle Barros, J.J., Carral, L., 2022. Numerical and Experimental Analysis of the Velocity Field Inside an Artificial Reef. Application to the Ares-Betanzos Estuary. JMSE 10, 1827. https://doi.org/10.3390/jmse10121827

Shu, A., Qin, J., Rubinato, M., Sun, T., Wang, M., Wang, S., Wang, L., Zhu, J., Zhu, F., 2021. An Experimental Investigation of Turbulence Features Induced by Typical Artificial M-Shaped Unit Reefs. Applied Sciences 11, 1393. https://doi.org/10.3390/app11041393

SimScale, 2025. K-Omega Turbulence Models.

Stake, J.L., Sammarco, P.W., 2003. Effects of pressure on swimming behavior in planula larvae of the coral Porites astreoides (Cnidaria, Scleractinia). Journal of Experimental Marine Biology and Ecology 288, 181–201. https://doi.org/10.1016/S0022-0981(03)00018-2

Sun, H., Yang, Q., Dong, J., Li, J., Chen, C., Tang, X., Zhang, Y., Ling, J., 2025. Comprehensive assessment of chemical and microbial inducers for coral larval settlement across diverse coral species. Front. Mar. Sci. 12, 1581753. https://doi.org/10.3389/fmars.2025.1581753

Sutton, M., Kippax-Chui, O., 2026. Coral Reef Lagrangian Settlement Simulator (CorLSS). https://doi.org/10.5281/ZENODO.23478962

Unity, 2025.

Vivier, B., Dauvin, J.-C., Navon, M., Rusig, A.-M., Mussio, I., Orvain, F., Boutouil, M., Claquin, P., 2021. Marine artificial reefs, a meta-analysis of their design, objectives and effectiveness. Global Ecology and Conservation 27, e01538. https://doi.org/10.1016/j.gecco.2021.e01538

Wang, X., Liu, X., Tang, Y., Zhao, F., Luo, Y., 2021. Numerical Analysis of the Flow Effect of the Menger-Type Artificial Reefs with Different Void Space Complexity Indices. Symmetry 13, 1040. https://doi.org/10.3390/sym13061040

Weller, H.G., Tabor, G., Jasak, H., Fureby, C., 1998. A tensorial approach to computational continuum mechanics using object-oriented techniques. Computers in Physics 12, 620–631. https://doi.org/10.1063/1.168744

Woo, J., Kim, D., Yoon, H.-S., Na, W.-B., 2014. Characterizing Korean general artificial reefs by drag coefficients. Ocean Engineering 82, 105–114. https://doi.org/10.1016/j.oceaneng.2014.02.025

Xia, X., Li, Y., Li, J., Gong, P., Huang, J., Lu, J., 2024. Effect of oyster shell filling in artificial reefs on flow field environment and assessing the potential of carbon fixation. Journal of Sea Research 202, 102537. https://doi.org/10.1016/j.seares.2024.102537

Yang, M., Tang, Y., Zhao, F., Yu, M., Wang, X., Liu, C., 2026. Optimizing Structural Parameters of Triangular Artificial Reefs for Enhanced Hydrodynamic Performance and Reduced Sediment Scour. Journal of Offshore Mechanics and Arctic Engineering 148, 031202. https://doi.org/10.1115/1.4070925

Zhang, J., Zhu, L., Liang, Z., Sun, L., Nie, Z., Wang, J., Xie, W., Jiang, Z., 2021. Numerical Study of Efficiency Indices to Evaluate the Effect of Layout Mode of Artificial Reef Unit on Flow Field. JMSE 9, 770. https://doi.org/10.3390/jmse9070770

Zhou, P., Gao, Y., Zheng, S., 2022. Three-dimensional numerical simulation on flow behavior behind trapezoidal artificial reefs. Ocean Engineering 266, 112899. https://doi.org/10.1016/j.oceaneng.2022.112899

Figure 1. Three-dimensional mesh representations of the fifteen artificial reefs used in this study. Scale bars indicate physical size. All meshes have a vertex density of approximately 1 vertex per cm, as visible from the vertex edges on each structure, where larger structures have a greater number of vertex edges.

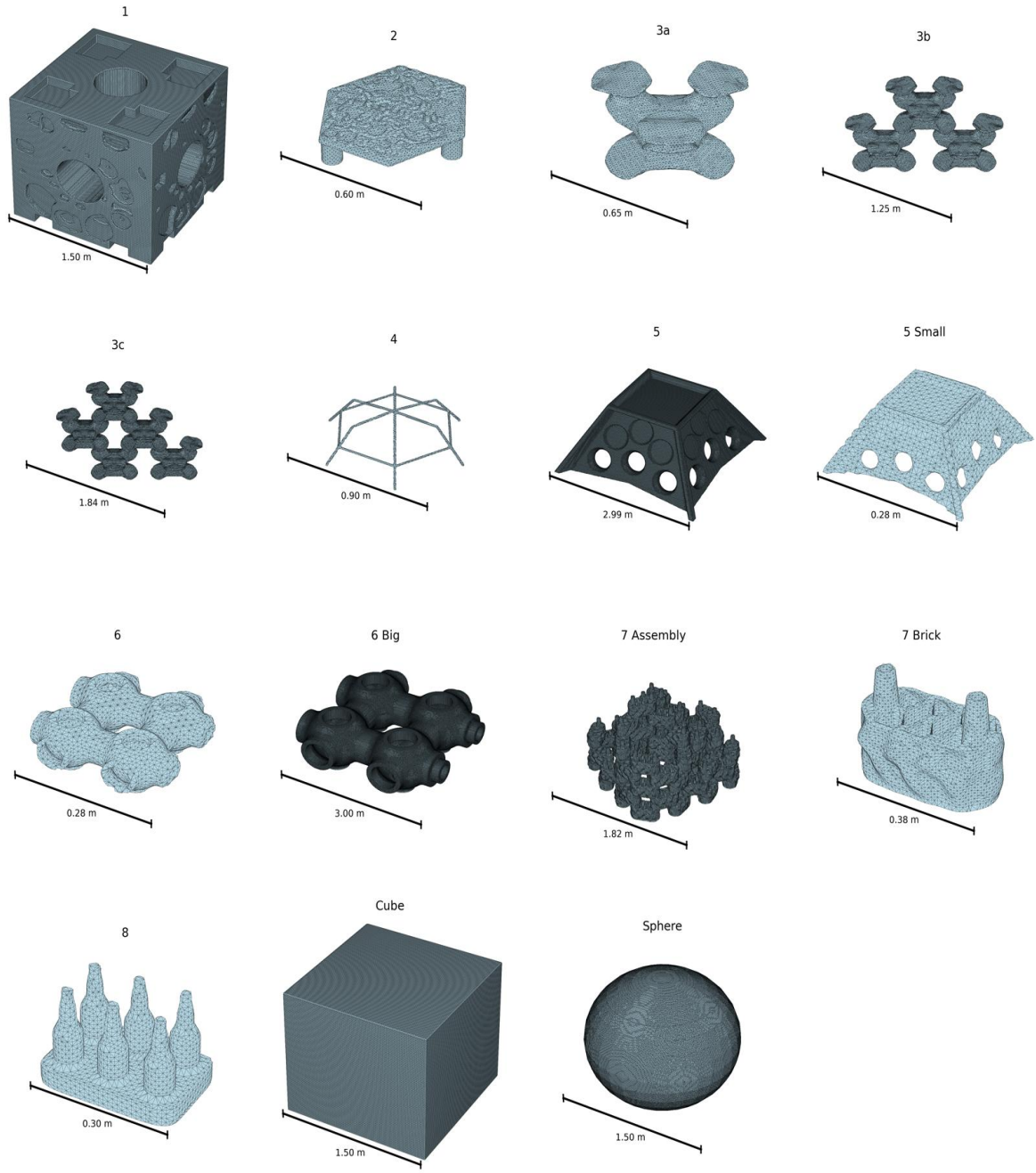

Figure 2. Three-dimensional visualisation of vertex-scale metrics for AR3a. a) Surface slope relative to vertical. b) Flow-facing angle between vertex normals and the streamwise direction. c) Relative curvature estimated from local vertex neighbours. d) Signed curvature, with red indicating concave and blue indicating convex regions. e) Euclidean distance to the nearest high-curvature vertex.

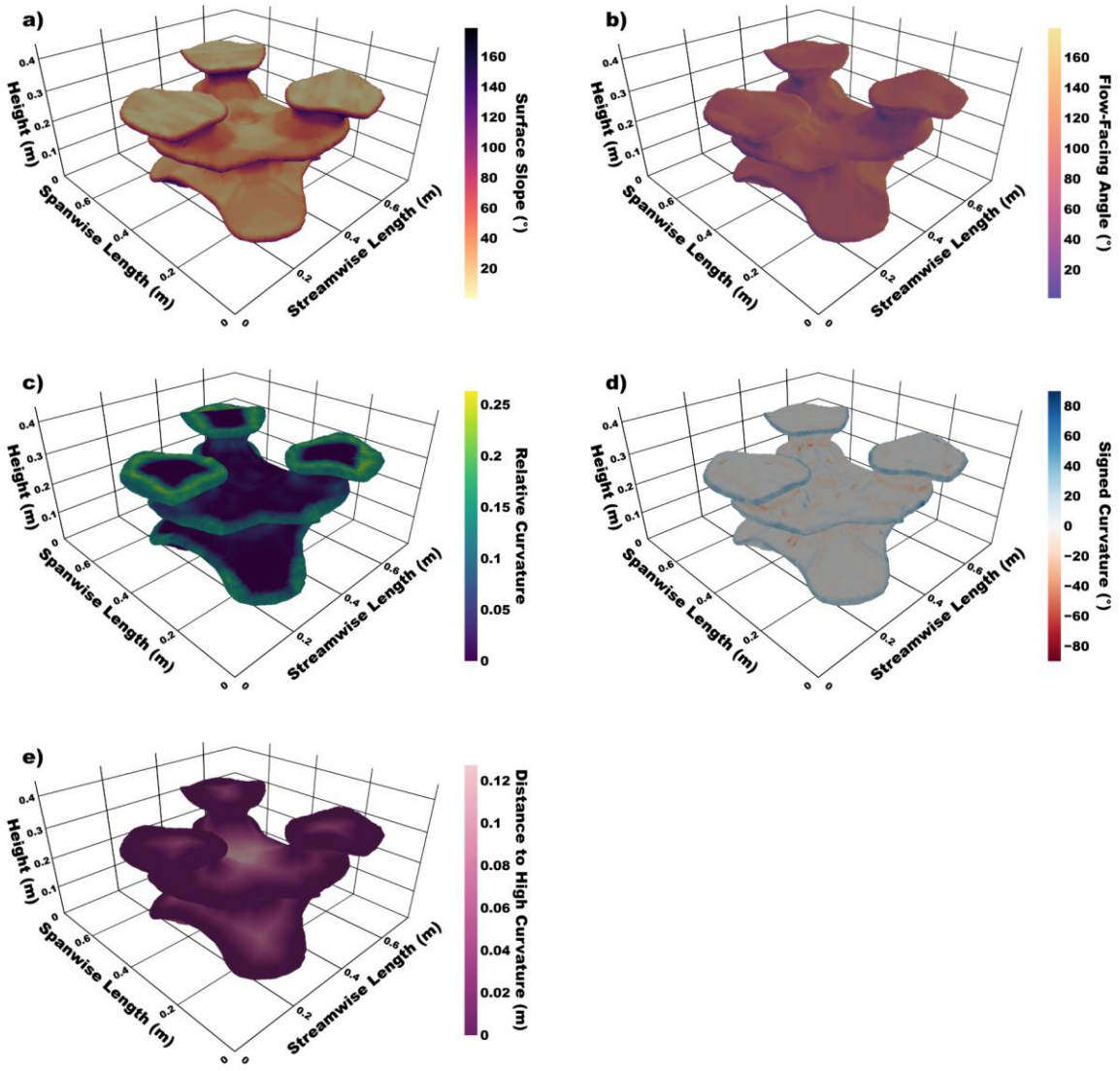

929 Figure 3, Bar graph showing the collision percentage for each AR at each angle it was
930 simulated at, including reference images of each AR.

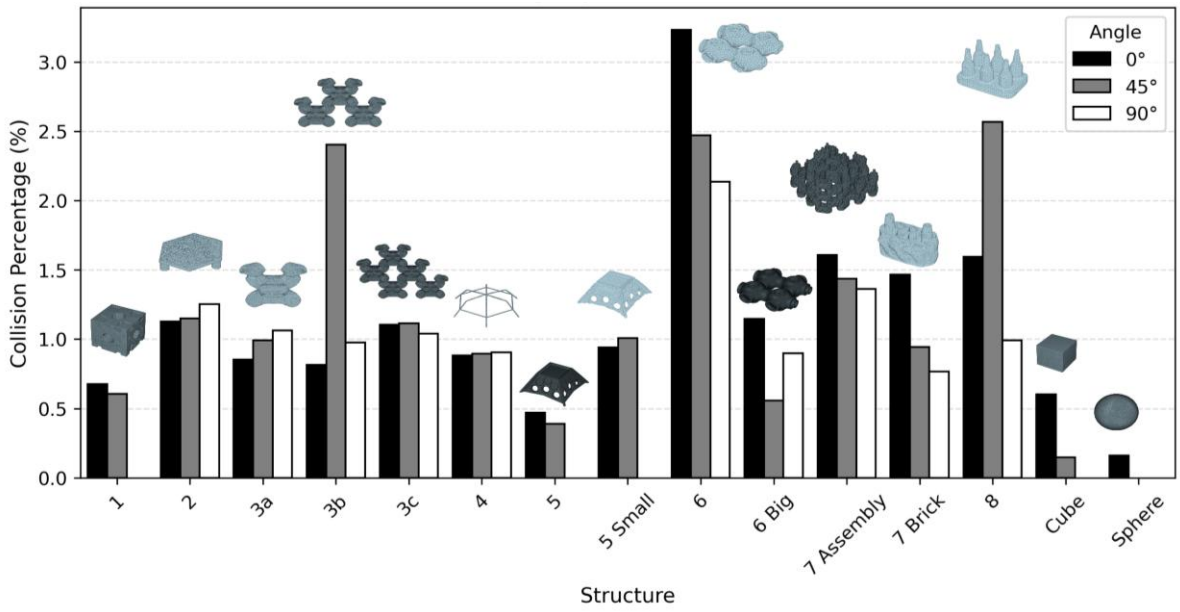

931
932

Figure 4, Collision percentage plotted against log10-transformed structure-scale mesh metrics for each artificial reef design. Mesh metrics are log transformed due to the large variance of scale between artificial reef sizes. Marker shape identifies the structure and marker fill indicates flow angle (black = 0°, grey = 45°, white = 90°). Dashed lines connect the different orientations of the same reef.

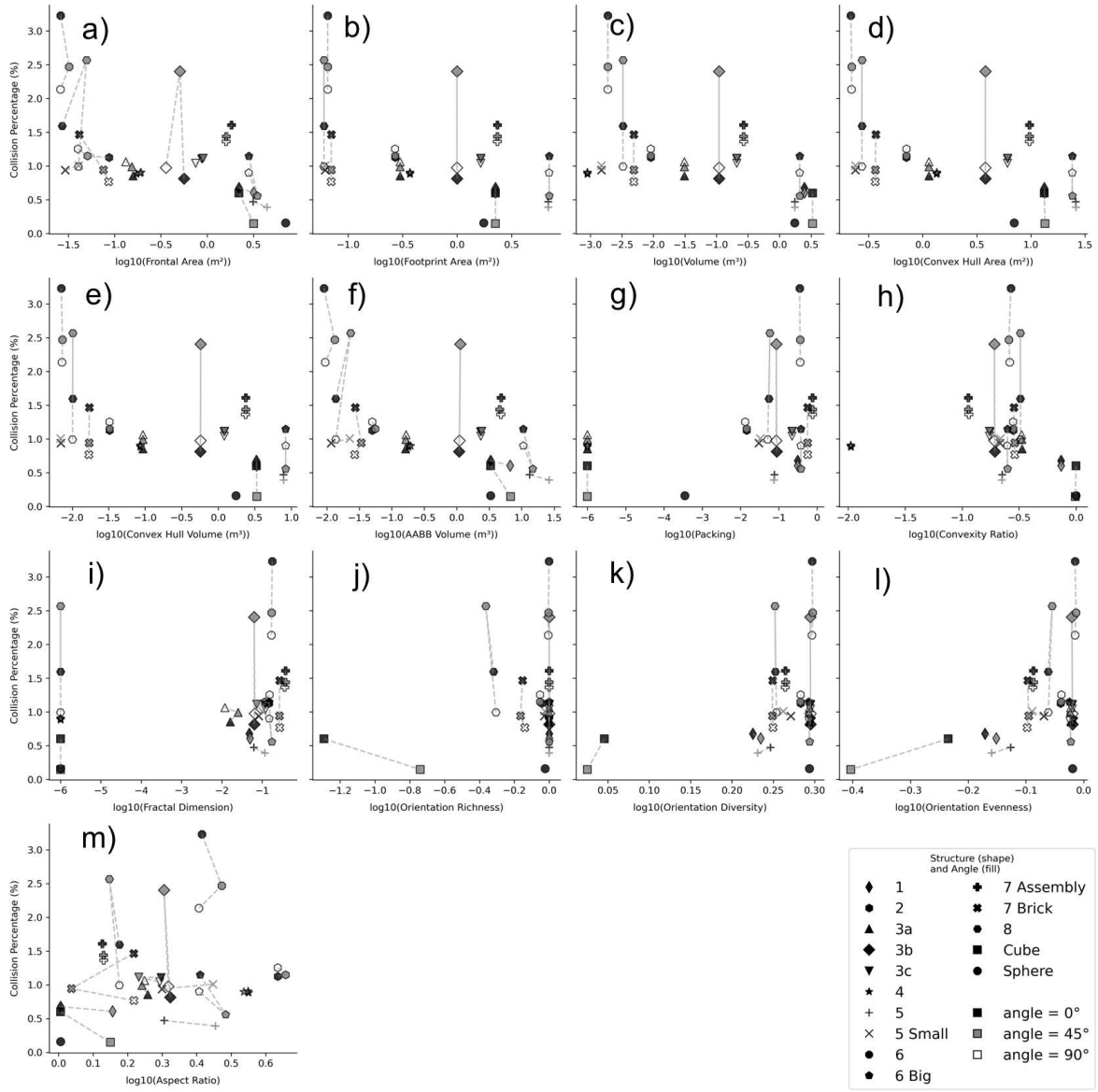

Figure 5, Spearman rank correlations between collision count and reef geometry at two scales. a) Structure-scale metrics and b) Vertex-scale metrics. Positive ρ indicates higher collision counts with increasing metric values, negative ρ indicates the opposite. The correlations do not adjust for repeated measures, and hence significance values are not provided.

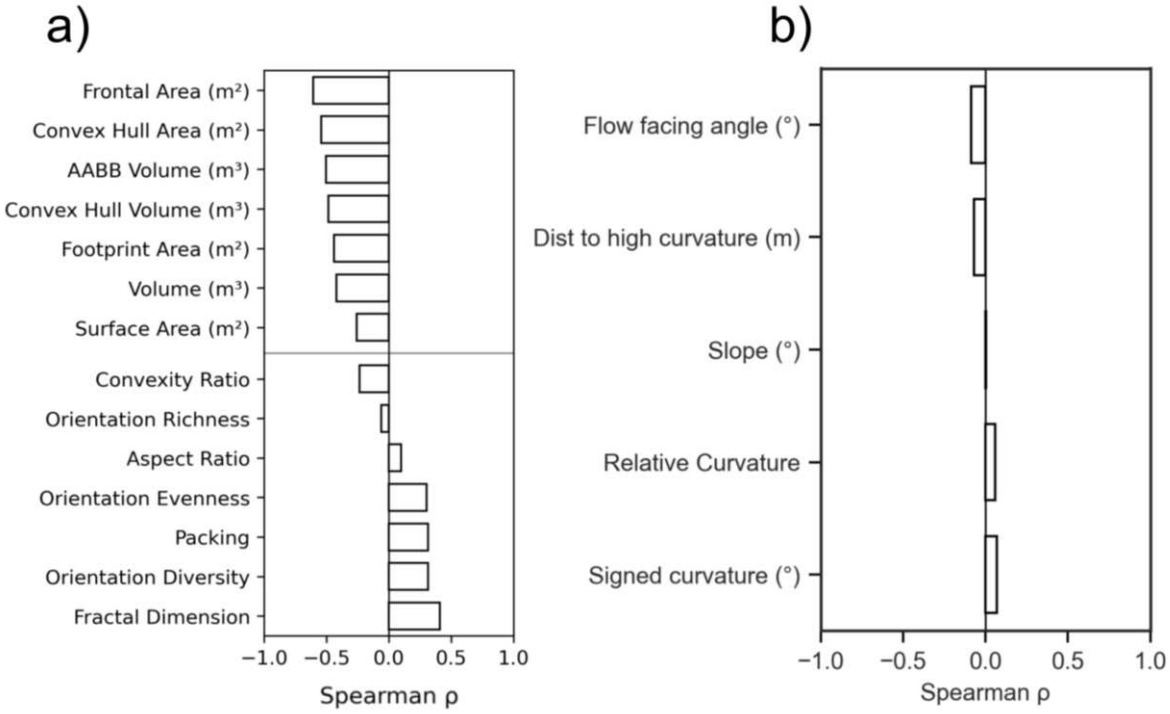

Figure 6, Normalised collision probability (total collisions in a bin divided by the number of vertices in that bin, left axis) against vertex-level complexity metrics. Data were binned into 30 equally spaced intervals for each feature. (a) Surface slope, (b) flow-facing angle, (c) relative curvature, (d) distance to high-curvature regions in meters, (e) signed curvature in degrees. Grey bars mark bins with fewer than 100 collisions. The dark-red line shows the number of vertices in each bin (right axis).

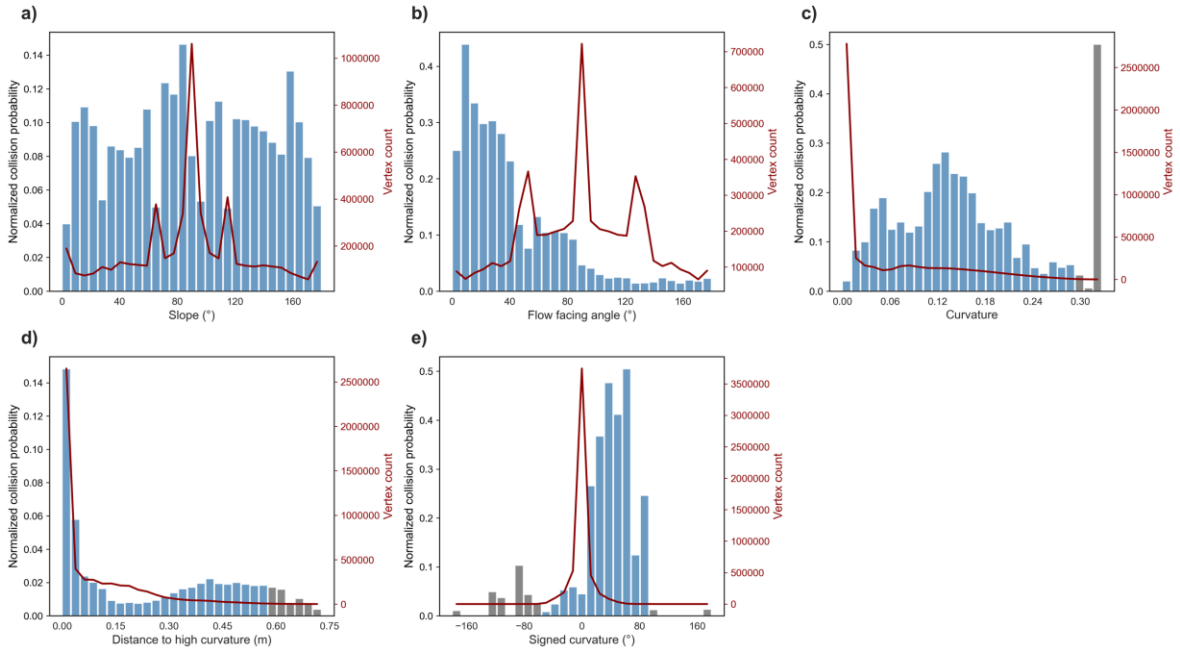

Figure 7. Interaction between surface curvature and flow on AR 7 Brick at 90° orientation. (a) Vertex-scale signed curvature mapped onto the three-dimensional mesh (red = convex, blue = concave, white = locally flat), with recorded particle collisions overlaid as red dots. (b) Top-down view of the CFD-simulated flow field around the same reef. Arrows indicate the direction of flow, and the colour scalar represents velocity magnitude (warmer colours = higher speed).

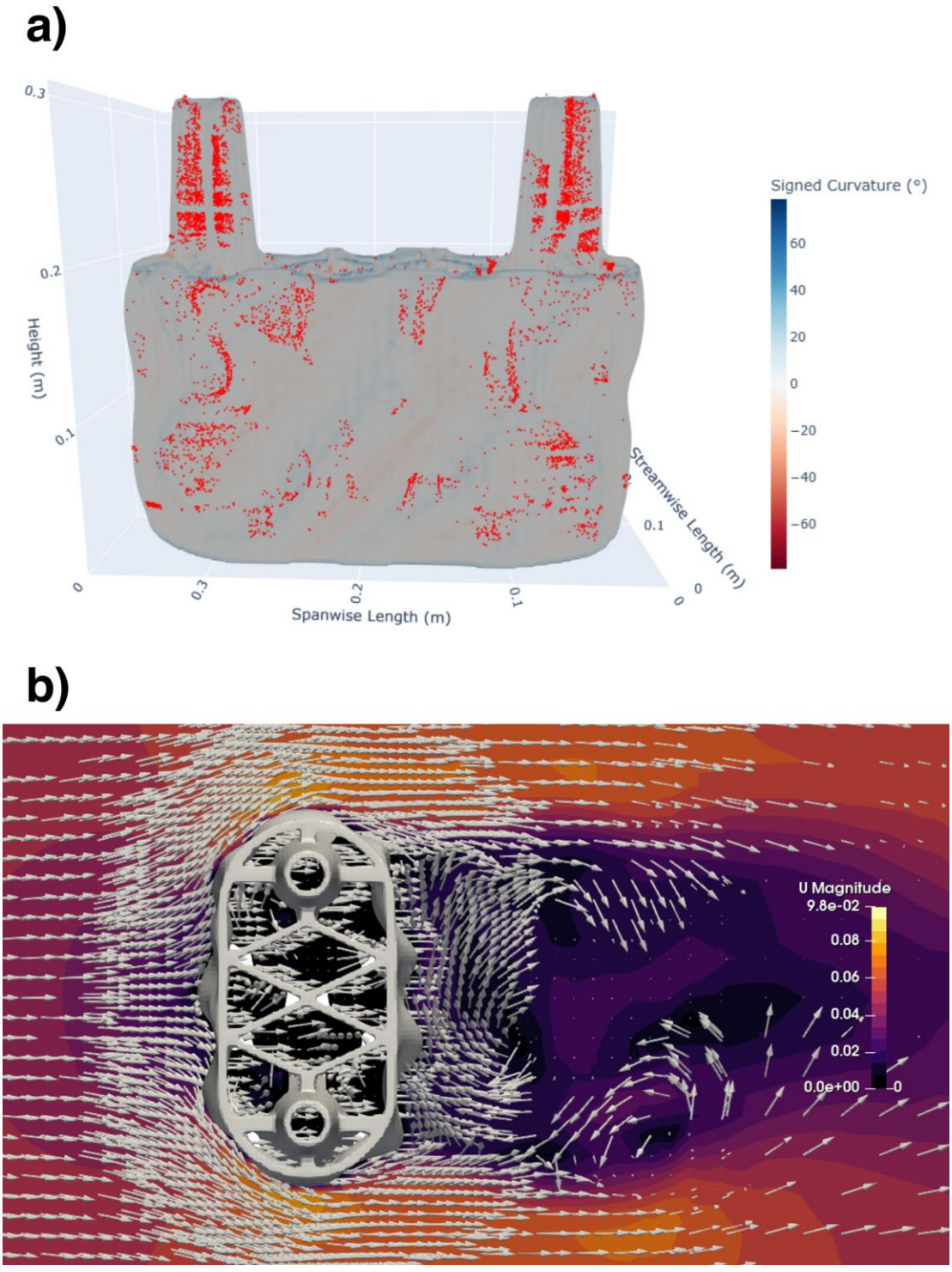

Appendix 1, Input and output parameters measured from Artificial Reefs used to calculate the computation fluid dynamics simulation domain and tracer particle simulation parameters. Categories merely organise the metrics into similar groups and do not represent inputs or outputs in the spreadsheet, only the metrics represent inputs and outputs. Input metrics are in clear cells and output metrics are in grey cells.

Category	Metrics	Derivation Method	Derivation Purpose
Artificial Reef Structural measurements	Streamwise Length (m) Span wise Length (m) Height (m)	Calculated in Blender by observing the ARs XYZ dimensions	Calculate the dimensions of the CFD domain and particle tracer simulation parameters as outlined below
	Projected Area (m^2)	In Blender the AR is flattened in the streamwise direction, and the area of the flat surface facing the flow is measured	Calculate hydraulic diameter in Table 2
	Projected Perimeter (m)	Using the same flattened object from Projected Area, the perimeter is calculated	Calculate hydraulic diameter in Table 2
CFD Domain Parameters	Cell Scale (m)	Manually set to 0.16. 16cm was found to be the optimal starting cell size for the purposes of this study through iterative refinement sensitivity testing.	Calculate the number of cells in each direction of the CFD domain
	X Max (m) Y Max (m) Z Max (m)	X Max = Streamwise length × 6 Y Max = Spanwise length × 5	Set the size of the domain for each CFD

		Z Max = Height × 5	simulation, and to calculate the Cell Count using the Cell Scale
	X Cell Count Y Cell Count Z Cell Count	X Cell Count = X Max / Cell Scale Y Cell Count = Y Max / Cell Scale Z Cell Count = Z Max / Cell Scale	Set the number of cells in the CFD domain in each direction before the resolution is increased near the AR
	X Position in Domain (m) Y Position in Domain (m)	X Position in Domain = Streamwise length × 2.5 Y Position in Domain = Y Max / 2	Calculate where the AR centre point sits within the CFD domain.
	Inlet Velocity (m/s)	0.05	Set the constant velocity of the incoming flow into the CFD domain
	Seconds to Clear Domain	= X Max / Inlet Velocity	Find how long to run the CFD simulation for

	Seconds to Run Simulation	= Seconds to Clear Domain × 3 In cases where this value is below 400 seconds, it was set to 400 seconds as in testing this appeared to be the minimum timesteps required to observe turbulent convergence	Input as the runtime for the CFD simulation.
Particle Tracer Simulation Parameters	Particle Kill Plane Location (m)	= X Max – 0.2	Set the X position in the particle tracer simulation where all particles exiting the domain are deleted from active memory
	Particle Spawn Point Origin (m)	= Y Position in Domain – Streamwise Length X and Z axis are kept consistent at just after the inlet at X= 0.1 and just above ground level at Z= 0.02	Find the origin position on the Y axis that particles will be released across
	Y Axis Particle Spawn Distance (m)	= Spanwise Length × 2	Find the distance from the Particle Spawn Point Origin in the Y axis that the particles will be released across

	Z Axis Particle Spawn Distance (m)	= Height × 1.5	Find the distance from the Particle Spawn Point Origin in the Z axis that the particles will be released across

969

970

Appendix 2, Input and output parameters for case specific CFD simulations, used to find the initial conditions of the fluid using openFOAM's kωSST pimpleFoam volume of fluid CFD solver. Input metrics are in clear cells and output metrics are in grey cells.

Metric	Derivation Method	Derivation Purpose
Flow velocity (m/s)	Set to 0.05 to match the inlet velocity	Reference velocity to calculate Reynolds Number and TurbulentKE
Density (kg/m^3)	Set to 1022 to match 30°C seawater	Calculate Kinematic Viscosity
Dynamic Viscosity (kg/m×s)	Set to 0.00087 to match 30°C seawater	Calculate Kinematic Viscosity
Kinematic Viscosity (m^2/s)	= Dynamic Viscosity / Density	Calculate Reynolds Number
Object Length (m)	Set to the streamwise Length of the reference AR for the specific case in Table 1	Calculate the Turbulent Length Scale and deltaT
Projected Area (m^2)	Set to the Projected Area of the reference AR for the specific case in Table 1	Calculate Hydraulic Diameter
Projected Perimeter (m)	Set to the Projected Perimeter of the reference AR for the specific case in Table 1	Calculate Hydraulic Diameter
Hydraulic Diameter (m)	= 4 × (Projected Area / Projected Perimeter)	Calculate Reynolds Number
blockMesh Scale	Set to 1 to represent the smallest intended cell size of 1cm	Calculate deltaT

blockMesh Cells	Set to the number of cells in the streamwise direction as calculated in Table 1	Calculate deltaT
Reynolds Number	= (Flow Velocity × Hydraulic Diameter) / Kinematic Viscosity	Determine if flow conditions are expected to be laminar or turbulent
Wall Turbulence Intensity	Set to 0.05 to represent 5% that is used as a standard	Calculate TurbulentKE
Turbulent Length Scale	= 0.07 × Object Length Where 7% is a standard fraction of a reference length of an object being used	Calculate turbulentOmega
TurbulentKE (Turbulent Kinetic Energy)	= 1.5 × (Object Length × Wall Turbulence Intensity)^2	Set the Turbulent Kinetic Energy value in the initialisation documentation and to calculate Turbulent Omega
TurbulentOmega	= (TurbulentKE)$^{0.5}$ / ($0.09^{0.25}$) × Turbulent Length Scale Where 0.09 is a constant	Set the TurbulentOmega value in the initialisation documentation
maxdeltaT (s)	Set to an initial conservative value of 0.001 while the simulation ramps up, allowing it to automatically adjust up to the estimated maxdeltaT, where: maxDeltaT = ((Maximum Courant Number × ((Object Length × blockMesh Scale) / blockMesh Cells)) / Flow Velocity)	Estimate the upper limit of timestep interval time that can be simulated for a case.

	Maximum courant number is limited to 0.5 to maintain the accuracy of the output	

974

Supplementary Files

This is a list of supplementary files associated with this preprint. Click to download.

- Appendix.docx